Cross Coupling of a Solid-State Qubit to an Input Signal due to Multiplexed Dispersive Readout

Dmitri Pitsun,[1] Aydar Sultanov,[1,*] Ilya Novikov,[1] Evgeniya Mutsenik,[1] Boris Ivanov,[1]
Aleksey Matanin,[2] Viktor Polozov,[3] Elizaveta Malevannaya,[3] Anton Ivanov,[2,3] Gleb Fedorov,[4,5,6]
Kaveh Delfanazari,[7,8,9,†] Ilya Rodionov,[2,3] and Evgeni Il'ichev[10,5,‡]

[1]*Faculty of Physical Engineering, Novosibirsk State Technical University, Novosibirsk 630073, Russia*

[2]*FMN Laboratory, Bauman Moscow State Technical University, Moscow 105005, Russia*

[3]*Dukhov Automatics Research Institute, (VNIIA), Moscow 127055, Russia*

[4]*National University of Science and Technology MISIS, Moscow 119049, Russia*

[5]*Russian Quantum Center, Skolkovo 121205, Russia*

[6]*Moscow Institute of Physics and Technology, Dolgoprudny 141701, Russia*

[7]*Electrical Engineering Division, University of Cambridge, Cambridge CB3 0FA, United Kingdom*

[8]*Cavendish Laboratory, University of Cambridge, Cambridge CB3 0HE, United Kingdom*

[9]*James Watt School of Engineering, University of Glasgow, Glasgow G12 8QQ, United Kingdom*

[10]*Leibniz Institute of Photonic Technology, Jena 07745, Germany*

The integration, scale-up, and multiplexing arrays of superconducting qubits in quantum circuits are the main challenges of superconducting quantum technology. Here we experimentally investigate the solid-state qubit multiplexing readout scheme, containing coplanar quarter-wavelength resonators coupled with a planar Xmon-type qubit, connected to a common coplanar transmission line. We find that the qubit energy spectrum is modified in the presence of an additional exciting signal at the fundamental frequency of the neighboring resonators. We attribute the origin of this effect to the electromagnetic field propagating through the common ground plane, which changes the qubit's characteristics. Our finding may be useful for the development of scalable superconducting quantum integrated circuits with arrays of multiplexed or coupled qubits for applications in superconducting quantum processing and computing.

I. INTRODUCTION

Recently, measurements of the dynamical characteristics of superconducting qubits have become a routine task in the era of quantum science and technology. During the last 20 years, their decoherence time has been significantly increased from several nanoseconds [1] to more than 100 μs [2]. These "optimistic" values encourage scientists and engineers to realize quantum-information-processing devices. However, scaling up and addressing the individual qubits in multiqubit integrated circuits is challenging [3–10]. In suggested designs, the dispersive readout scheme is used: the qubit is coupled to a resonator, and its state is defined by the resonator frequency shift [11,12].

To reduce the number of readout lines, a frequency multiplexing control system for a multiqubit scheme has been proposed [3,4]. In such an approach, the signals, which address different readout resonators, are sent to a common

transmission line, which is coupled to resonators with the qubits. Since each resonator has a different fundamental frequency, their bandwidths ought to be smaller than the frequency differences between them.

For multiplexing designs, it is usually supposed that the qubit interacts only with its own resonator unless otherwise provided by architecture [6,8,9]. However, in practice, a number of interactions of various orders between superconducting-circuit elements are observed due to the crosstalk effects. For example, it is well known that there is crosstalk between qubits in neighboring resonators [13], as well as unwanted coupling between resonators [14]. Such crosstalk can change the qubit states and its eigenfrequencies (qubit transition frequency between the ground $|g\rangle$, excited $|e\rangle$, and higher states), leading to a shift of resonance frequencies of on-chip qubit-resonator systems. Inherently, according to these changes, the crosstalk effect can be experimentally characterized.

In this paper, we experimentally study quantum circuits containing a (flux-tuned) Xmon qubit. The qubit eigenfrequencies are measured directly by two-tone spectroscopy. In this standard technique, two simultaneous microwave

---
*sultanov.aydar.nstu@gmail.com

†kd398@cam.ac.uk

‡evgeni.ilichev@leibniz-ipht.de

signals are used to locate the frequency of the qubit transition. This is performed by feeding a weak probing tone at the resonance frequency of the cavity while sweeping the frequency of the second (driving) tone, close to the estimated qubit's frequency. When close enough to the qubit eigenfrequency, the qubit is driven out of the ground state and into an incoherent mixed state by the drive tone. Owing to the dispersive shift, the amplitude dip and phase shift are observed in the readout transmission signal [15–17].

Since this consequence depends on the input microwave signals, the following effects are also considered and measured by two-tone spectroscopy, and by direct measurement of the transmission characteristics of the resonator at different powers of the probing signal:

(a) The ac Stark shift (it is well known that for a qubit-resonator system the qubit eigenfrequency depends on the resonator photon population [18,19]).

(b) Kinetic inductance [the fundamental frequency of thin-film resonators (up to 100 nm) also depends on the power of the microwave signal due to the change in their kinetic inductance [20,21]].

We measure the dependence of the eigenfrequency of the Xmon qubit [22] on the chip on additionally applied signals of various frequencies and powers. We show that the variation of the qubit eigenfrequency is caused by neither an ac Stark shift nor a change of the film kinetic inductance. We attribute the origin of these effects to the electromagnetic field, which propagates through the common ground plane and changes the qubit's characteristics.

II. EXPERIMENTAL RESULTS

To investigate the details and features of the multiplexing readout scheme, and also to estimate the influence of the aforementioned effects, we design and fabricate a single chip containing a superconducting open coplanar waveguide, which is capacitively coupled to seven high-quality quarter-wavelength resonators, including resonator f_{r4} with its Xmon qubit (see Figs. 1 and 2).

The open coplanar waveguide is used to guide rf signals into the chip. As shown in Fig. 2, the qubit represents an interferometer loop shunted by the capacitance C_x. Part 6 in the chip (see Fig. 1) is not used, and instead a global flux-bias coil is used to tune the Xmon-qubit energy. The process for fabrication of the chip included an epitaxial aluminum (Al) ground plane with a thickness of 100 nm. The root-mean-square surface roughness of the superconducting Al thin film is less than 0.8 nm, and we did not expect any observable Al film grains [23]. The sheet kinetic inductance of the Al film is approximately 0.05 pH/□, which corresponds to a London penetration depth of approximately 50 nm, a value expected for high-quality superconducting films. The coplanar waveguide and resonators are patterned and fabricated by electron-beam lithography and dry etching in a Cl-based plasma, followed by electron-beam shadow evaporation of an Al-Al_2O_3-Al Josephson junction (JJ) in a UHV evaporation system [24]. The deposition of the JJ bottom electrode is preceded by an *in situ* Ar-ion milling to remove the native oxide of the Al ground plane. The tunnel barrier of the JJ is formed in the same high-vacuum cycle in pure oxygen. A schematic diagram of the superconducting quantum circuit on the chip and information about the resonators are provided in Fig. 2.
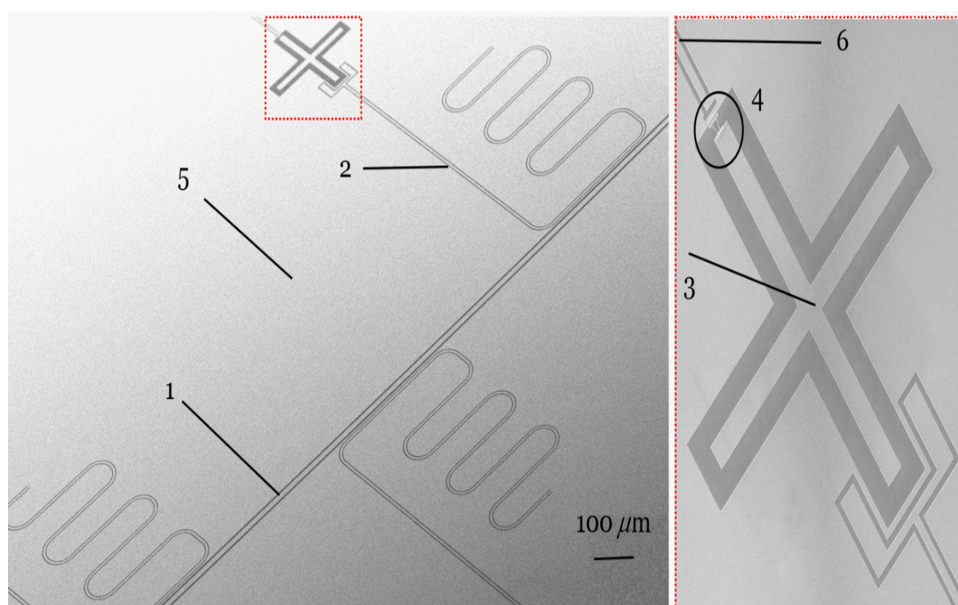

FIG. 1. SEM image of our superconducting quantum circuit showing part of the device with three resonators (left). The Xmon qubit (dashed red square) is coupled to the direct resonator under study (see Fig. 2 for more details). 1, open coplanar waveguide (equivalent to C_l and L_l discussed in Fig. 2); 2, quarter-wavelength resonator; 3, shunting qubit capacitance (C_x); 4, two-Josephson-junction-interferometer placements; 5, common ground plane; 6, individual flux-bias line of qubit eigenfrequency.

Schematic of the integrated superconducting multi-resonator chip with Xmon qubit

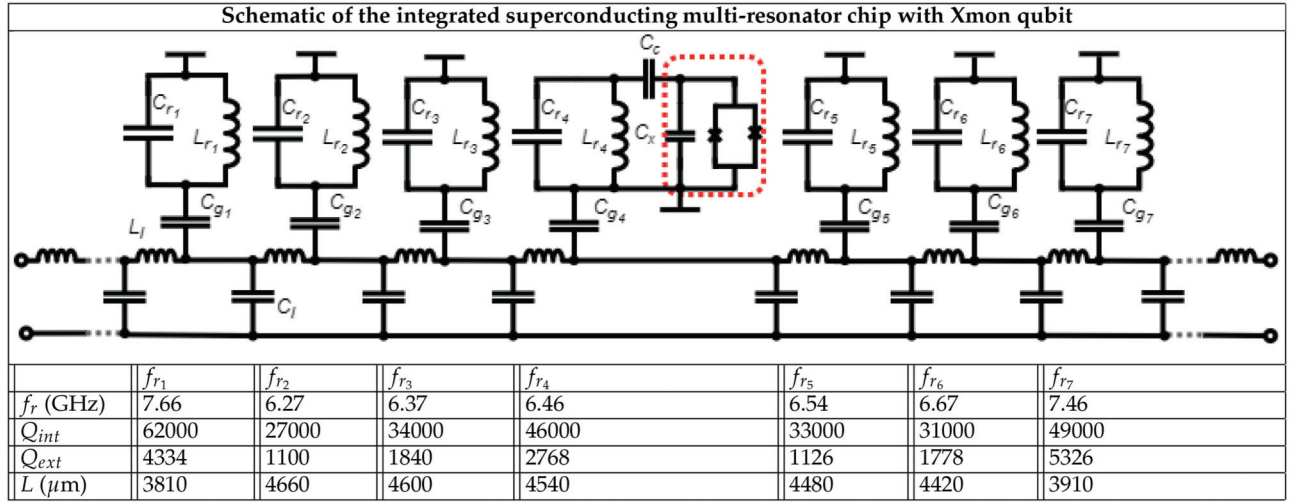|		f_{r_1}	f_{r_2}	f_{r_3}	f_{r_4}		f_{r_5}	f_{r_6}	f_{r_7}
f_r (GHz)		7.66	6.27	6.37	6.46		6.54	6.67	7.46
Q_{int}		62000	27000	34000	46000		33000	31000	49000
Q_{ext}		4334	1100	1840	2768		1126	1778	5326
L (μm)		3810	4660	4600	4540		4480	4420	3910

FIG. 2. Layout of the superconducting quantum device and summary of the important information regarding the resonators: resonance frequency (f_r), internal quality factor (Q_{int}), external quality factor (Q_{ext}), and length (L). In all resonators, the coplanar waveguide has a width of 7.6 μm and a gap of 3.4 μm.

L_l and C_l are the open coplanar waveguide's inductance and capacitance per unit length, L_{r_i} and C_{r_i} denote the inductance and capacitance of the resonators in the lumped-element representation (here $i = 1$–7), which are capacitively coupled to the open coplanar waveguide through the capacitances C_{g_i}, and the qubit is coupled to the f_{r_4} resonator through the coupling capacitor C_c. The loop with two crosses (JJs) forms the interferometer, which is shunted to the ground plane through the capacitance C_x.

The resonators measured for crosstalk investigation are $f_{r_2}, f_{r_4}, f_{r_6}$, and f_{r_7}. The Xmon qubit is coupled to the fourth resonator f_{r_4}, which is named the "direct resonator" here (the other resonators are called "indirect" for this qubit). Since the numerical estimation of the crosstalk effect can be obtained from the variation of the qubit eigenfrequency, we implement two-tone-spectroscopy measurements (for more details, see Appendix A).

We apply two signals: (i) a driving signal with power P_{dr} and frequency f_{dr} and (ii) a probing signal with power P_{pr} and frequency f_{pr}. Figure 3(a) shows an example of the measurement results. The qubit's first eigenfrequency, corresponding to the $|g\rangle$-$|e\rangle$ transition, is 5.8 GHz at the sweet spot. The second one, corresponding to the $|e\rangle$-$|f\rangle$ transition, is 5.5 GHz at the sweet spot. The horizontal line in Fig. 3(a) represents the direct resonator's fundamental resonance frequency f_{r_4}.

To rule out two important physical effects, ac Stark shift and kinetic inductance change, we perform additional experiments.

We measure the ac Stark shift of the qubit's first eigenfrequency. For a fixed value of the current in the flux-bias coil ($I = 148$ μA), fixed frequency of the probing signal (f_{pr}), and fixed value of the driving power $P_{dr} = -107$ dBm, we sweep the probing power P_{pr} and measure the

qubit's eigenfrequency. This power P_{pr} defines the average microwave photon number in the direct resonator, and the value of the ac Stark shift. Since the probing signal is applied to the direct resonator f_{r_4}, the average photon number N_{av} in this resonator can be roughly estimated according to Eq. (9) from Refs. [25,26]:

$$N_{av} = \frac{\left(2C_{g_4} V_{in} V_n\right)^2}{h^2 \left[2\left(f_{r_4} - f_{sig}\right)^2 + \Gamma^2\right]}, \quad (1)$$

where C_{g_4} is the coupling capacitance between the direct resonator and the open coplanar waveguide, and Γ is the coupling constant between the direct resonator and the open coplanar waveguide. Both constants are estimated numerically from the sample design, resulting in $C_{g_4} = 14$ fF and $\Gamma = 4.4$ MHz. V_{in} corresponds to the voltage amplitude of the signal at the frequency $f_{sig} = f_{r_4}$ applied to the circuit input (from 100 nV to 3 μV), and $V_n = \sqrt{hf_{r_4}/C_{r_4}}$ is the zero-point voltage in the resonator at the resonance frequency f_{r_4} (order of magnitude of microvolts), C_{r_4} is the capacitance of the resonator, and h is Planck's constant.

Figure 3(b) presents the dependence of the shift of the frequency of the $|g\rangle$-$|e\rangle$ transition on the probing power. It shows the ac Stark shift of the Xmon qubit for fixed driving power $P_{dr} = -107$ dBm. Here the y axis is the power of the probing signal in terms of the average number of photons in the f_{r_4} resonator, and the x axis is the driving-signal frequency. The dashed white line shows the chosen value of the number of photons ($N = 100$) populating the resonator with the qubit for the crosstalk investigation. From Fig. 3(b), it is seen that the probing-signal power corresponding to around $N = 100$ photons does not show any
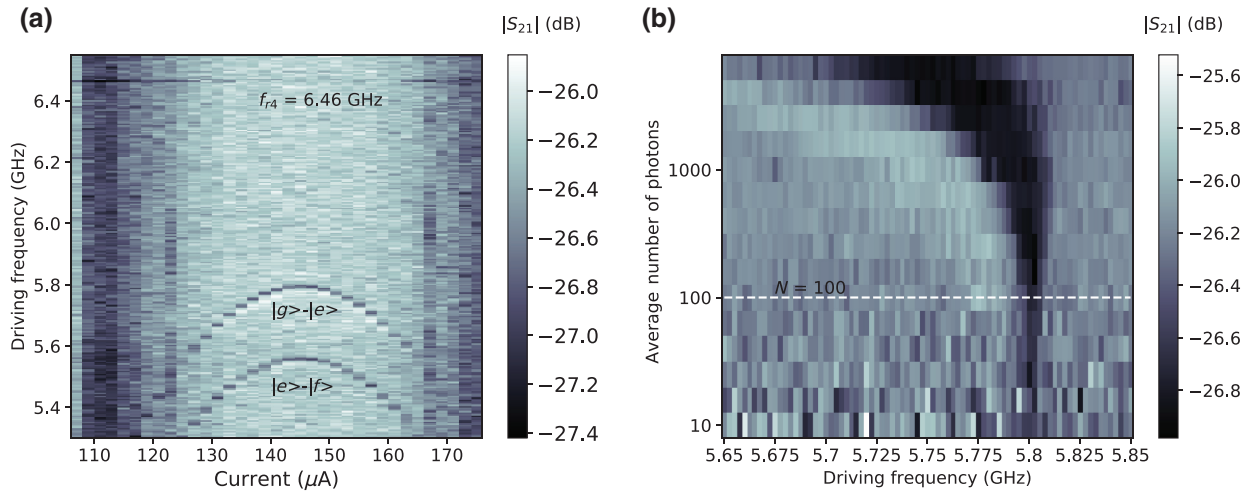
FIG. 3. (a) Two-tone-spectroscopy results for $P_{pr} = -117$ dBm, $P_{dr} = -107$ dBm, and $f_{pr} = f_{r_4}$. In the graph, the y axis is the driving-signal frequency, and the x axis is the current in the flux-bias coil. (b) The ac Stark shift of the Xmon qubit, for fixed driving power $P_{dr} = -107$ dBm and $f_{pr} = f_{r_4}$. Here the left y axis is the power of the probing signal in terms of average number of photons in resonator f_{r_4}. The right y axis is the power of the probing signal at the input of the chip, and the x axis is the driving-signal frequency. The dashed white line shows the chosen value of number of photons ($N = 100$) populating the resonator with the Xmon qubit (f_{r_4}) for the crosstalk investigation.

significant shift of the frequency of $|g\rangle$-$|e\rangle$ transition (low-photon-number mode). For the following experiments, the probing power is fixed at this value, $P_{pr} = -117$ dBm.

Since the ac Stark shift also depends on the detuning between the qubit and the direct resonator, the resonator's frequency shift caused by kinetic inductance change should also be considered.

The kinetic inductance in such superconducting quantum circuits depends on the applied power. Since in our measurement the probing power is fixed at $P_{pr} = -117$ dBm, to reconstruct the kinetic inductance an additional tone is applied. We measure the transmission $|S_{21}|$ of a probing signal in a narrow frequency range at $f - f_{r_4}$ which is equal to ± 10 MHz with the presence of this additional tone (f_{th}). Then f_{th} is applied at the frequencies $f_{r_2} = 6.27$ GHz and $f_{r_6} = 6.67$ GHz with powers $P_{th} = -74$ dBm and $P_{th} = -92$ dBm, respectively. For these experiments, the qubit is detuned far away from the resonator's frequency. This allows us to define the frequency change of only the "bare" resonator with minimal qubit impact since the qubit-resonator interaction can be ignored. The results are shown in Fig. 4. Although the additional tones are detuned far from the direct resonator's frequency, they will still have a slight influence on it. This is because of the finite quality factor of the direct resonator. There is also the slight shift in the background level; we are uncertain of its origin of this effect at this stage but we believe it does not alter the main results. Therefore, in this way we can estimate the influence of the additional tones on the resonator's spectrum, which causes a direct resonator's frequency shift of less than 2.5 MHz.

We can also estimate the maximum shift of the qubit from the ac Stark shift and kinetic inductance change, wherein the qubit-excitation- frequency shift does not exceed 5 MHz, which is the value of a standard shift (see Figs. 3 and 4).

To study the crosstalk effect, we apply a third microwave-signal tone (with the same input line) with frequency f_{th} and power P_{th} from the second generator, denoted as "rf gen 2" (see Appendix A). The electromagnetic field distribution of the third tone depends on its frequency f_{th}. If f_{th} corresponds to one of the quarter-wavelength resonator's resonance frequencies, we observe the electric field maximum at the open end of that resonator. By use of our setup (see Appendix A), we measure the eigenfrequency of our flux-tuned Xmon qubit as a function of the third-tone parameters; that is frequency and power (f_{th} and P_{th}).

The third microwave tone is applied at the indirect resonance frequencies ($f_{r_2}, f_{r_6}, f_{r_7}$) and outside the bandwidth of the resonators (we label them here as f_{out1} and f_{out2}). Examples of two-tone-spectroscopy results with the third tone applied at $f_{th} = f_{r_7} = 7.46$ GHz are shown in Fig. 5. The main feature which allows us to distinguish the crosstalk effect from the ac Stark effect is that we do not observe any significant increase of the eigenfrequency-level width (one can compare it with the results presented in Fig. 3). For example, at third-tone power -104 dBm, the width is 10.8 MHz, while it is 13 MHz for a power of -92 dBm. The eigenfrequency-level width measured in the absence of the third tone changes from 10 to 60 MHz for even-lower power ranges, as shown in Fig. 3(b).
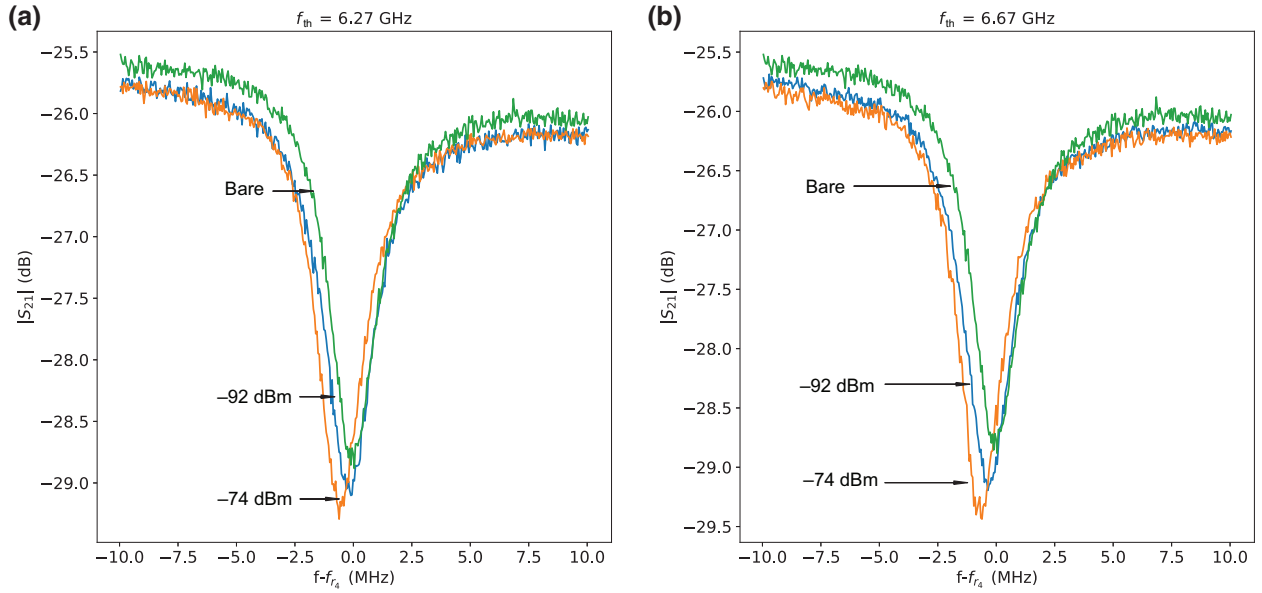
FIG. 4.   Transmission $|S_{21}|$ of resonator f_{r_4} in the presence of additional tones at frequencies $f_{th} = f_{r2} = 6.27$ GHz (a) and $f_{r_6} = 6.67$ GHz (b) for additional tone powers $P_{th} = -92$ dBm (blue line) and $P_{th} = -74$ dBm (orange line). The green line corresponds to the transmission without an additional tone ("bare" resonator). The probing power is $P_{pr} = -117$ dBm (corresponding to $N = 100$ photons in resonator f_{r_4}).

Figure 5 shows that the qubit eigenfrequency decreases due to the applied third tone. It can be inferred from the Fig. 5 that as the power of the third tone is increased, the noise increases. This effect is beyond the scope of this work and will be reported elsewhere.

The qubit eigenfrequencies (levels) at the sweet spot are found from vertical cut lines. These cut lines presented in Fig. 5 for two-tone-spectroscopy measurements of the qubit with the third tone applied at four different powers ($P_{th} = -94, -84, -80$, and -74 dBm) are shown in Fig. 9 in Appendix B. We see that despite noise growth as the power increases, it is still possible to define the qubit eigenfrequency, but at maximum power $P_{th} = -74$ dBm, the $|e\rangle$-$|f\rangle$ level is not seen.

The qubit eigenfrequency, extracted from the two-tone-spectroscopy measurements, depending on the third-tone power conveyed in the average number of photons populating resonator f_{r_4} is shown in Fig. 6. Since the direct resonator has a finite quality factor, the electromagnetic fields generated at other frequencies (i.e., at $f_{r_2}, f_{r_6}, f_{r_7}, f_{out1}$, and f_{out2}) decay faster. The average number of photons can be estimated from Eq. (1) by substitution of f_{sig} and V_{in} into the corresponding frequency and amplitude of the third tone. The gray area shows the qubit-eigenfrequency shift caused by the ac Stark effect. The shift originating from the kinetic inductance is not shown here because it is much smaller than the ac Stark shifts.

From Figs. 5 and 6 it is clearly inferred that the qubit-eigenfrequency shift due to the third tone exceeds the values estimated above by assumptions of the ac Stark

effect and thin-film kinetic inductance effect. Moreover, for an average number of photons of 100, the shift is much larger than that in the ac-Stark-shift experiment. Also, we observe a smaller shift for the frequencies outside the bands of on-chip resonators. These frequencies are exactly equal to f_{out1} and f_{out2}. At these frequencies the microwave fields propagate mainly through the central open coplanar waveguide; nevertheless, because of the finite quality factors of the resonators, some power flows into them and the effect remains visible. In the next section, we present the detailed analysis of the measurement results.

III. DISCUSSION

As discussed already, the frequency of qubit transition $|g\rangle$-$|e\rangle$ in the presence of a microwave field can be changed according to the following mechanisms:

(a) The ac Stark shift: in this case, the interaction between the qubit and the photon field leads to renormalization of the qubit's frequency by the an amount of approximately [27–29]

$$\sim \frac{\lambda^2 E_C}{\left(\Omega_q - \omega_r\right)\left(\Omega_q - \omega_r - E_C\right)} N_{ph}, \qquad (2)$$

where λ is the coupling constant of the qubit and photons at frequency $\omega_r = 2\pi f_r$, N_{ph} is the average number of photons of the field, Ω_q is the frequency of the qubit transition $|g\rangle - |e\rangle$, and E_C is the Coulomb energy of the qubit.
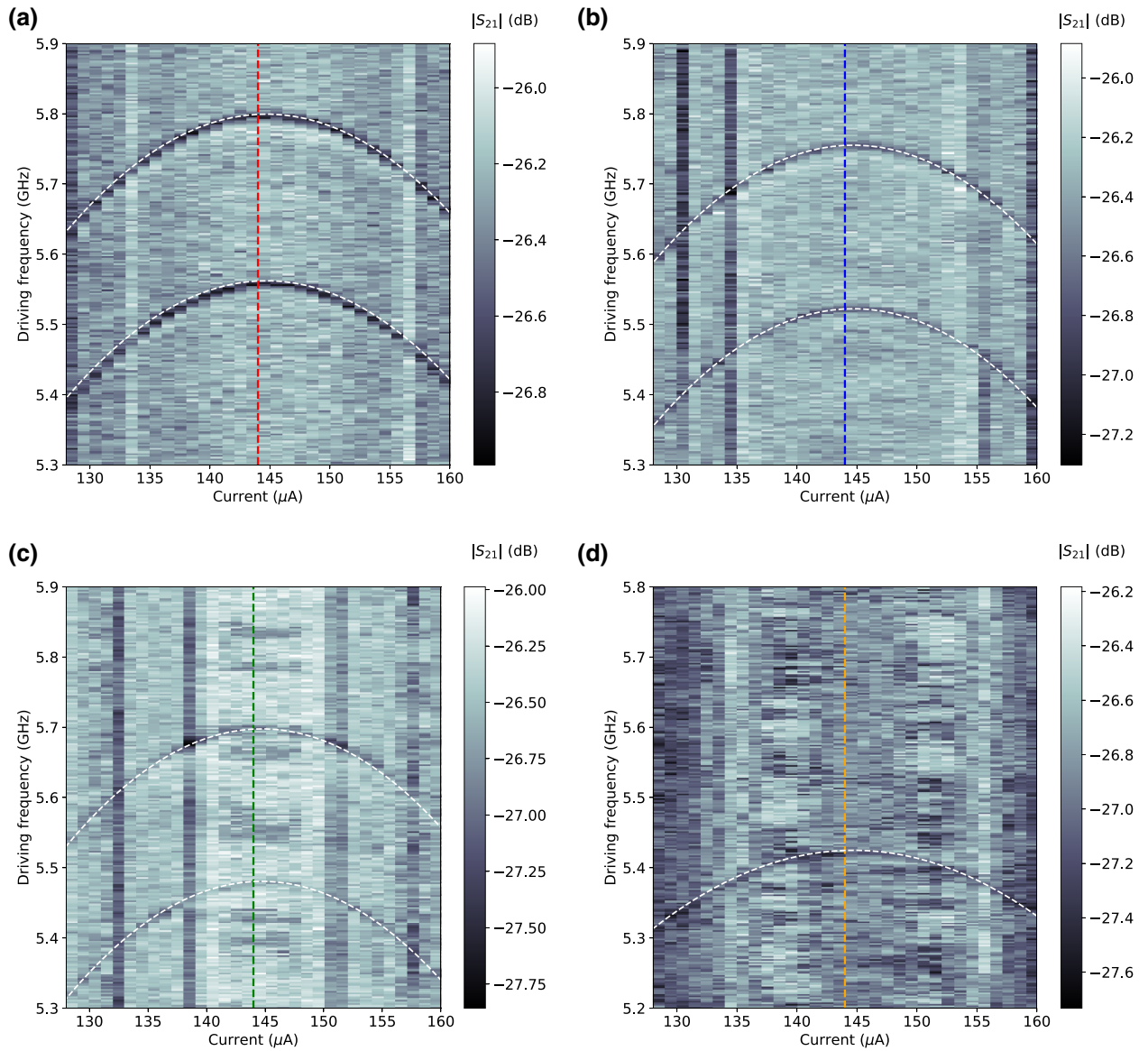
FIG. 5. Two-tone-spectroscopy measurement with the third tone ($f_{th} = f_{r_7} = 7.46$ GHz) applied with powers $P_{th} = -94$ dBm (a), $P_{th} = -84$ dBm (b), $P_{th} = -80$ dBm (c), and $P_{th} = -74$ dBm (d). The vertical lines show areas presented in Fig. 9. The power increase of the third tone causes a downshift of the qubit's eigenlevels.

(b) Thin-film kinetic inductance change: here, current propagating on the surface of the superconducting thin film changes the linear electrical parameters of the coplanar line according to the following equation [17]:

$$f_r \sim \frac{1}{\sqrt{(L_r + L_{\text{kin}})\, C_r}}, \qquad (3)$$

where L_r and C_r are the linear electrical inductance and capacitance of the resonator, respectively, which are identified by the line geometry in a small-current operation regime, and $L_{\text{kin}} \sim (I/I_c)^2$, where I_c is the critical current of the thin film. Increase of the thin-film current amplitude I leads to a decrease of the resonance frequency (see

Fig. 4). As the observed kinetic inductance effect is small even for resonator f_{r4}, the qubit frequency should not be affected.

However, the experimentally observed shift of the qubit eigenfrequency is much larger than that predicted by the two aforementioned effects. Let us assume that the observed shifts can be explained by the ac Stark mechanism caused by interaction between the qubit and the photons of the third tone existing in the direct resonator. The shift is inversely proportional to the detuning between the photons of the third tone and qubit frequencies [see Eq. (2)]. This means that with increasing detuning between the qubit and the third tone, this shift should decrease. For example, the shift caused by the third tone at $f_{r_7} = 7.46$
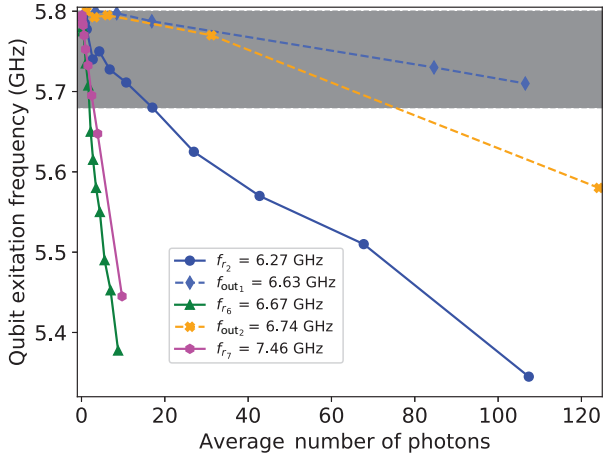
FIG. 6. Dependence of the qubit eigenfrequency on the third-tone photon number in resonator f_{r_4} at on-chip resonators frequencies $f_{r_2} = 6.27$ GHz (solid blue line), $f_{r_6} = 6.67$ GHz (solid green line), and $f_{r_7} = 7.46$ GHz (solid pink line) as well as at frequencies out of the bands of the on-chip resonators of $f_{out1} = 6.63$ GHz (dashed light-blue line) and $f_{out2} = 6.74$ GHz (dashed orange line). The gray area depicts the qubit-eigenfrequency shift caused by the ac Stark effect. The shift originating from the kinetic inductance is not shown here because it is much smaller than the ac Stark shifts.

GHz should be smaller than the shift caused by the probe signal at $f_{r_4} = 6.46$ GHz when the average numbers of photons N_{ph} are equal.

Moreover, increasing the detuning results in a decrease of the average number of photons N_{ph} with third tone's frequency in the direct resonator where the Xmon qubit is placed. This suggests that, from this point of view, the as Stark shift should decrease. Besides, the current amplitude I [see Eq. (3)] of the superconducting thin film should also decrease. Since we experimentally observe a completely different behavior, as Fig. 6 shows, we conclude that the assumption that the qubit interacts only with the electromagnetic field in resonator f_{r_4} is likely not to be the case. Indeed, a strong resonance dependence of the qubit eigenfrequency on the third tone's frequency in Fig. 6 indicates the presence of an additional mechanism.

To clarify this issue, it is quite natural to assume that this mechanism is related to the sample design. As shown in Fig. 1, in our superconducting circuit, the two-Josephson-junction interferometer is shunted to the ground plane over the cross capacitance. The third-tone currents excite corresponding microwave fields in the ground plane, and the currents caused by these fields propagate near the interferometer ring and thereby cause a variation of the interferometer Josephson energy E_J. Figure 7 summarizes the suppression of the Josephson energy of the qubit by the third-tone power, obtained from the eigenfrequency variation.

As expected, this effect is stronger for frequencies that are in resonance with on-chip resonators ($f_{r_2}, f_{r_6}, f_{r_7}$) and

weaker for those without resonance frequencies (f_{out1}, f_{out2}) as shown in Fig. 6. The propagating fields with frequencies f_{out1}, and f_{out2} do not penetrate significantly into the ground plane. Also, one can estimate the Josephson-energy variation that is necessary for a shift of the frequency of the qubit transition $|g\rangle - |e\rangle$ of 400 MHz. This shift is the maximum value that can be estimated from Fig. 6. According to the results from Ref. [29], for this type of qubit design, the capacitance of the cross capacitor C_x is about 80 fF, which gives us an estimation that the change in the Josephson energy is about 10%.

Such a change is due to suppression of the critical current, by the high-frequency current, in the Josephson junctions [30–32] and has a "quadratic" dependence on the current amplitude. Here we apply the simplified model of the suppression of the critical current by a microwave field with frequency $\omega_r = 2\pi f_{rf}$ and amplitude I_{rf}, taking into account the Bessel-form dependence of the critical current on the field parameters, which gives the exact solution for $\hbar\omega_{rf} \gg 2qR_N I_0$:

$$
\begin{aligned}
E_J &= \frac{\Phi_0 I_c^{qb}}{2\pi}, \\
I_c^{qb} &= I_0 \left(1 - \gamma I_{rf}^2\right), \\
\gamma &= \frac{1}{4I_0^2\Omega}, \\
\Omega &= \frac{\hbar\omega_{rf}}{2qR_N I_0},
\end{aligned}
\tag{4}
$$

where the Josephson energy of the qubit depends on the critical current of the interferometer I_c^{qb}, and I_c^{qb} depends on the suppression of the critical current by the microwave field, defined by γ and Ω, which describe the sensitivity of interferometer to the field. I_0 is the interferometer critical current in the absence of the microwave field, and is given by $I_0 = 2I_{JJ} \cos(2\pi \Phi/\Phi_0)$. In this equation I_{JJ} is the critical current of the Josephson junction with normal-state resistance $2R_N$, Φ is the external flux, Φ_0 is the flux quantum, $\hbar$ is the reduced Planck's constant and q is the electron charge. Extracting all the characteristics of the fabrication process and the design topologies, we calculate the qubit parameters to be as follows: the shunt capacitance is 80 fF, the critical current in two-Josephson-junction interferometer is $2I_{JJ} = 40$ nA, and the normal-state resistance R_N is 7 kΩ. The variation of the Josephson energy caused by the microwave power is calculated from Eq. (4) and is shown in Fig. 7. Disparities between the theoretical fits and experimental data are explained by the violation of the inequality $\hbar\omega_{rf} \gg 2qR_N I_0$; nevertheless qualitatively they are in good agreement.

The applied powers of the third tone are quite high in comparison with ones used for single-qubit characterization experiments. Firstly, the effect is easier to observe and
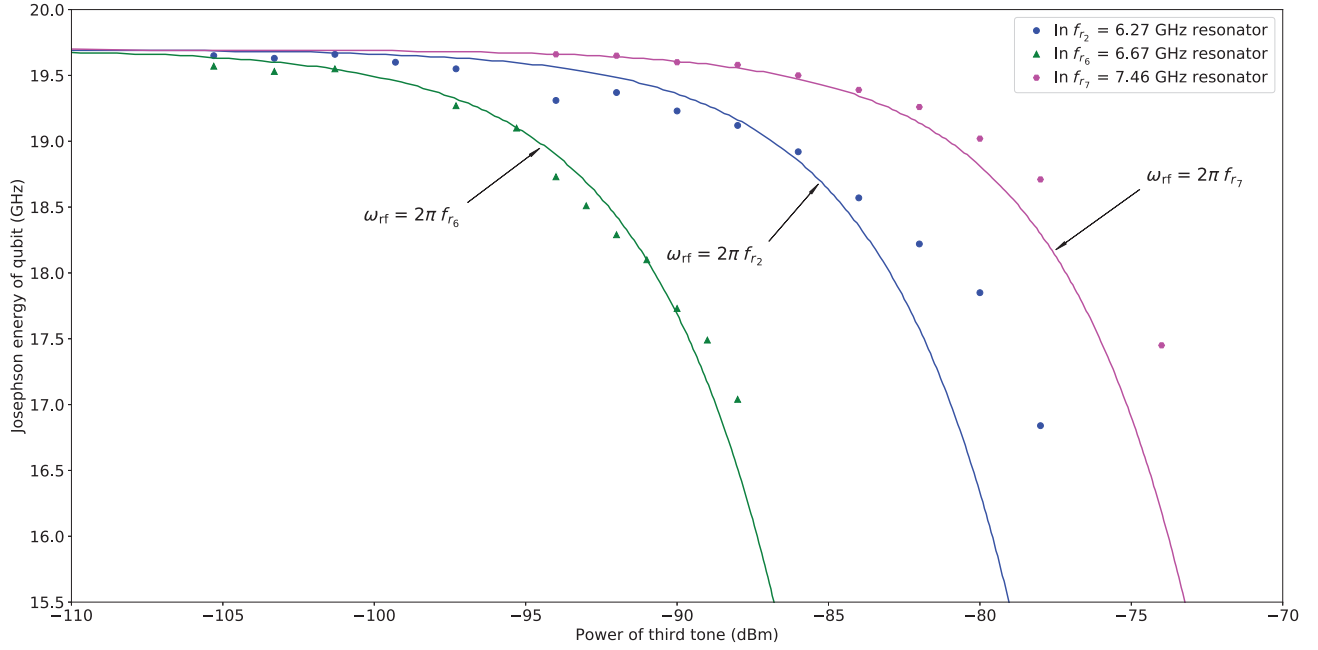
FIG. 7. Variation of the Josephson energy as a function of the third-tone power P_{th} (x axis) for three different frequencies: $f_{r_2} = 6.27$ GHz, $f_{r_6} = 6.67$ GHz, and $f_{r_7} = 7.46$ GHz. Here dots are the experimental data, and the solid lines are the fits to the experimental data obtained with Eq. (4). The qubit eigenfrequency is defined by the Coulomb and Josephson energies; the latter decreases under crosstalk radiation, coming from resonators f_{r_2}, f_{r_6}, and f_{r_7}.

here we depict just the existence of the interaction channel between artificial surroundings on the chip and the qubit. Secondly, in a case of multiqubit systems, when readout signals are applied to several qubits, the total power increases linearly, and this effect should be taken into account. Moreover, some readout schemes use Jaynes-Cummings interaction nonlinearity at high powers [33].

Simplifying, one can say that the two-Josephson-junction interferometer is mainly subjected to microwave radiation from different sources, which are located at various positions on the chip and have radiation frequencies coincident with the frequencies of the on-chip resonators. The path between these sources and the two-contact interferometer imposes some attenuation of the microwave power reaching the interferometer. The x axis in Fig. 7 shows the microwave-field power reaching the interferometer, which is calculated from the equation $10 \log\left[(I_{rf}^2/1 \text{ mW}) \times 50 \, \Omega\right] + A_{sys} + A_{f_{rf}}$ with use of the standard relation between power and current. These additional fitting parameters $\text{Att}_{f_{rf}}$ are attenuations, and for three different frequencies, $f_{r_2} = 6.27$ GHz, $f_{r_6} = 6.67$ GHz, and $f_{r_7} = 7.46$ GHz, are calculated to be $\text{Att}_{6.27\text{GHz}} = 50$ dB, $\text{Att}_{6.67 \text{ GHz}} = 40$ dB, and $\text{Att}_{7.46\text{GHz}} = 55$ dB, respectively. Similar attenuation values (around 60 dB) were reported in Ref. [34], where the value of the attenuation coefficient was mostly defined by the chip geometry. To avoid having this kind of attenuation in superconducting multiqubit circuits, one of possible improvement could be the development of a general model for calculating these attenuation coefficients so as to minimize the observed crosstalk effects.

IV. CONCLUSIONS

We provide the evidence of a crosstalk effect between an Xmon qubit and neighboring resonators, in addition to the well-known crosstalk between qubits, resonator, and control lines that has been previously studied. We attribute the origin of this effect to the electromagnetic field propagating through the common ground plane, which changes the qubit's characteristics. The microwave fields suppress the critical current of the Josephson junctions, leading to the qubit-eigenfrequency variation. Although we observe this effect at quite high powers of the third tone, this effect can play a significant role in superconducting multiqubit integrated circuits even at lower powers. To prevent the observation of such an effect in superconducting quantum circuits, it has to be taken into account when the device chip is being designed.
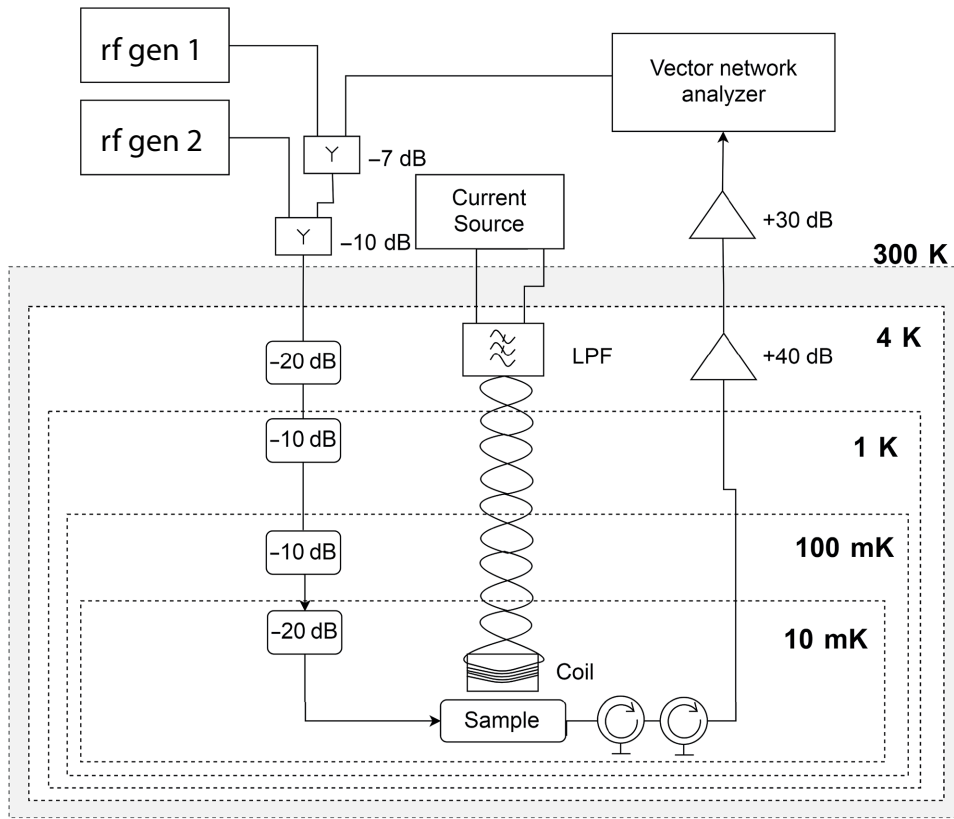
FIG. 8. The measurement setup: rf gen 1 and a vector network analyzer (VNA) are used for two-tone spectroscopy. The signal from the VNA is the probing signal with frequency f_{pr} and power P_{pr}, while the signal from rf gen 1, with frequency f_{dr} and power P_{dr}, is used to drive transitions between the qubit's eigenlevels. The third tone, with frequency f_{th} and power P_{th}, for the crosstalk investigation is generated by rf gen 2 . When f_{dr} coincides with one of the transitions, the transmission of the VNA signal is changed. In this way, two-tone spectroscopy provides information on the qubit eigenenergies, which are changed in the presence of signal generated by rf gen 2. LPF, low-pass filter.

APPENDIX A: THE SETUP

The experimental setup is shown in Fig. 8. The generator rf gen 1 and vector network analyzer produce two signals: (i) a driving signal with power P_{dr} and frequency f_{dr} and (ii) a probing signal with power P_{pr} and frequency f_{pr}. All the signals are attenuated by the value $A_{sys} = 87$ dB, which includes the attenuators at the input line, losses in power dividers (Y in Fig. 8), and losses in the input
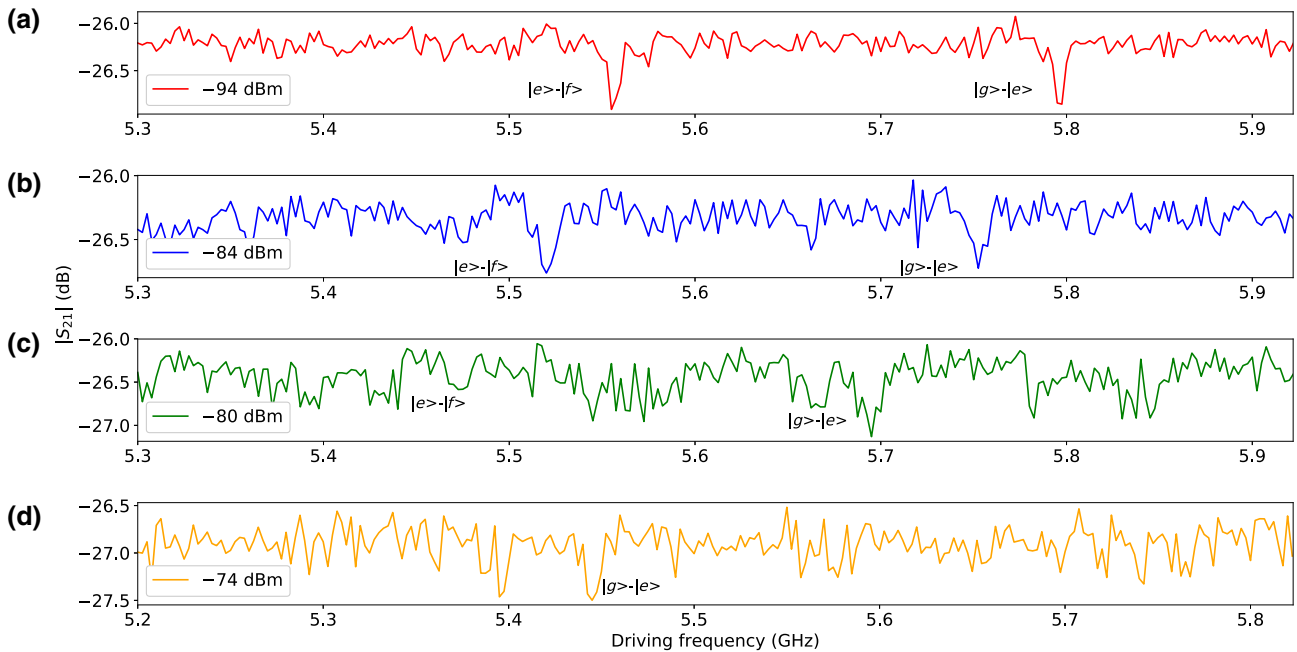

FIG. 9. Qubit eigenfrequencies, from two-tone-spectroscopy measurements, as a function of the applied third tone ($f_{r_7} = 7.46$ GHz) at four different powers: (a) $P_{th} = -94$ dBm, (b) $P_{th} = -84$ dBm, (c) $P_{th} = -80$ dBm, and (d) $P_{th} = -74$ dBm.

cables (around 10 dB for our frequency range). The generator rf gen 2 produces the third-tone signal with power P_{th} and frequency f_{th}. It is also used to introduce an additional tone for kinetic-inductance-shift measurements.

The measured signals at the device output are amplified at the 4-K stage by a cryogenic low-noise amplifier with a gain of 40 dB and sub-5-K noise temperature, followed by a room-temperature amplifier with power gain of 30 dB. The qubit excitation frequency is tuned by a dc flux bias applied to the interferometer's loop with use of an external superconducting Nb coil (marked "coil" in Fig. 8). To filter the qubit flux-bias line, we use a two-stage differential *RC* filter with a cut-off frequency of 10 kHz. The filter is placed at the 4-K stage.

In this experiment, the individual control line on the device chip is not used (position 6 in Fig. 1). The current in the flux-bias coil is set by a precision current source developed by our group, which can provide current of high accuracy for the qubit working point (it can generate current with dispersion and spectral current noise density of less than 10 nA and 1 nA/$\sqrt{\text{Hz}}$, respectively).

APPENDIX B: THE QUBIT'S EIGENFREQUENCY

Figure 9 shows the cut lines shown in Fig. 5 for the two-tone-spectroscopy measurements of the qubit with the third tone applied at four different powers: $P_{th} = -94$, -84, -80, and -74 dBm. Despite the noise increasing as the power increases, it is still possible to define the qubit's eigenfrequency $|g\rangle - |e\rangle$, but at maximum power, $P_{th} = -74$ dBm, the lower eigenfrequencies are not seen.

---

[1] Y. Nakamura, Yu. Pashkin, and J. S. Tsai, Coherent control of macroscopic quantum states in a single Cooper-pair box, Nature **398**, 786 (1999).

[2] C. Wang, C. Axline, Y. Y. Gao, T. Brecht, Y. Chu, L. Frunzio, M. H. Devoret, and R. J. Schoelkopf, Surface participation and dielectric loss in superconducting qubits, Appl. Phys. Lett. **107**, 162601 (2015).

[3] M. Jerger, S. Poletto, P. Macha, U. Hübner, A. Lukashenko, E. Il'ichev, and A. V. Ustinov, Readout of a qubit array via a single transmission line, Eur. Phys. Lett. , **96**, 40012 (2011).

[4] M. Jerger, S. Poletto, P. Macha, U. Hübner, E. Il'ichev, and A. V. Ustinov, Frequency division multiplexing readout and simultaneous manipulation of an array of flux qubits, Appl. Phys. Lett. **101**, 042604 (2012).

[5] L. DiCarlo, J. M. Chow, J. M. Gambetta, Lev S. Bishop, B. R. Johnson, D. I. Schuster, J. Majer, A. Blais, L. Frunzio, S. M. Girvin, and R. J. Schoelkopf, Demonstration of two-qubit algorithms with a superconducting quantum processor, Nature **460**, 240 (2009).

[6] J. Heinsoo, C. Andersen, A. Remm, S. Krinner, T. Walter, Y. Salathé, S. Gasparinett, J.-C. Besse, A. Potočnik, A. Wallraff, and C. Eichler, Rapid High-Fidelity Multiplexed Readout of Superconducting Qubits, Phys. Rev. Appl. **10**, 034040 (2018).

[7] J. Ikonen, J. Goetz, J. Ilves, A. M. Gunyho, M. Partanen, K. Y. Tan, D. Hazra, L. Grönberg, V. Vesterinen, S. Simbierowicz, J. Hassel, and M. Möttönen, Qubit Measurement by Multichannel Driving, Phys. Rev. Lett. **122**, 080503 (2019).

[8] M. Gong *et al.*, 12-Qubit Entanglement on a Superconducting Quantum Processor, Phys. Rev. Lett. **122**, 110501 (2019).

[9] M. Majer, J. M. Chow, J. M. Gambetta, J. Koch, B. R. Johnson, J. A. Schreier, L. Frunzio, D. I. Schuster, A. A. Houck, A. Wallraff, A. Blais, M. H. Devoret, S. M. Girvin, and R. J. Schoelkopf, Coupling superconducting qubits via a cavity bus, Nature **449**, 443 (2007).

[10] T. Wang, Z. Zhang, L. Xiang, Z. Jia, P. Duan, Z. Zong, Z. Sun, Z. Dong, J. Wu, Y. Yin, and G. Guo, Experimental Realization of a Fast controlled-Z Gate via a Shortcut to Adiabaticity, Phys. Rev. Appl. **11**, 034030 (2019).

[11] E. Il'ichev, N. Oukhanski, T. Wagner, H.-G. Meyer, A. Yu. Smirnov, M. Grajcar, A. Izmalkov, D. Born, W. Krech, and A. Zagoskin, Radio-frequency method for investigation of quantum properties of superconductingstructures, Low Temp. Phys. **30**, 620 (2004).

[12] D. Born, V. I. Shnyrkov, W. Krech, E. Il'ichev, M. Grajcar, U. Hübner, and H.-G. Meyer, Reading out the state inductively and microwave spectroscopy of an interferometer-type charge qubit, Phys. Rev. B **70**, 180501(R) (2004).

[13] P. Mandala, G. Zhang, T. Hazard, and A. Houck, Suppression of Qubit Crosstalk in a Tunable Coupling Superconducting Circuit, Phys. Rev. Appl. **12**, 054023 (2019).

[14] O. Noroozian, P. K. Day, B. H. Eom, H. G. Leduc, and J. Zmuidzinas, Crosstalk reduction for superconducting microwave resonator arrays, IEEE Trans. Microw. Theory Tech. **60**, 1235 (2012).

[15] A. Wallraf, D. I. Schuster, A. Blais, J. M Gambetta., J. Schreier, L. Frunzio, M. H. Devoret, S. M. Girvin, and R. J. Schoelkopf, Sideband Transitions and Two-Tone Spectroscopy of a Superconducting Qubit Strongly Coupled to an On-Chip Cavity, Phys. Rev. Lett. **99**, 050501 (2007).

[16] E. I. Kiselev, A. S. Averkin, M. V. Fistul, V. P. Koshelets, and A. V. Ustinov, Two-tone spectroscopy of a SQUID metamaterial in the nonlinear regime, Phys. Rev. Res. **1**, 033096 (2019).

[17] Y. Nakamura, H. Terai, K. Inomata, T. Yamamoto, W. Qiu, and Z. Wang, Superconducting qubits consisting of epitaxially grown NbN/AlN/NbN Josephson junctions, Appl. Phys. Lett. **99**, 212502 (2011).

[18] D. I. Schuster, A. Wallraff, A. Blais, L. Frunzio, R.-S. Huang, J. S. Majer, M. Girvin, and R. J Schoelkopf, AC Stark Shift and Dephasing of a Superconducting Qubit Strongly Coupled to a Cavity Field, Phys. Rev. Lett. **94**, 123602 (2005).

[19] J. Gambetta, A. Blais, D. I. Schuster, A. Wallraff, L. Frunzio, J. Majer, M. H. Devoret, S. M. Girvin, and R. J. Schoelkopf, Qubit-photon interactions in a cavity: Measurement-induced dephasing and number splitting, Phys. Rev. A **74**, 042318 (2006).

[20] K. Watanabe, K. Yoshida, T. Aoki, and S. Kohjiro, Kinetic inductance of superconducting coplanar waveguides, Jpn. J. Appl. **33**, 5708 (1994).

[21] J. M. Sage, V. Bolkhovsky, W. D. Oliver, B. Turek, and P. B. Welander, Study of loss in superconducting coplanar waveguide resonators, J. Appl. Phys. **109,** 063915 (2011).

[22] R. Barends, J. Kelly, A. Megrant, D. Sank, E. Jeffrey, Y. Chen, Y. Yin, B. Chiaro, J. Mutus, C. Neill, P. O'Malley, P. Roushan, J. Wenner, T. C. White, A. N. Cleland, and J. M. Martinis, Coherent Josephson Qubit Suitable for Scalable Quantum Integrated Circuit, Phys. Rev. Lett. **111,** 080502 (2013).

[23] I. A. Rodionov, A. S. Baburin, A. R. Gabidullin, S. S. Maklakov, S. Peters, I. A. Ryzhikov, and A. V. Andriyash, Quantum engineering of single-crystalline silver thin films, Sci. Rep. **10,** 867 (2019).

[24] G. J. Dolan, Offset masks for lift-off photoprocessing, Appl. Phys. Lett. **31,** 377 (1977).

[25] G. Oelsner and E. Il'ichev, Switching dynamics of an underdamped Josephson junction coupled to a microwave cavity, J. Low. Temp. **192,** 169 (2018).

[26] S. N. Shevchenko, G. Oelsner, Ya. S. Greenberg, P. Macha, D. S. Karpov, M. Grajcar, U. Hübner, A. N. Omelyanchouk, and E. Il'ichev, Amplification and attenuation of a probe signal by doubly dressed states, Phys. Rev. B **89,** 184504 (2014).

[27] R. Bianchetti, S. Filipp, M. Baur, J. M. Fink, M. Göppl, P. J. Leek, L. Steffen, A. Blais, and A. Wallraff, Dynamics of dispersive single-qubit readout in circuit quantum electrodynamics, Phys. Rev. A **80,** 043840 (2009).

[28] A. Blais, R-Sh. Huang, A. Wallraff, S. M. Girvin, and R. J. Schoelkopf, Cavity quantum electrodynamics for superconducting electrical circuits: An architecture for quantum computation, Phys. Rev. A **69,** 062320 (2004).

[29] J. Koch, T. M. Yu, J. Gambetta, A. A. Houck, D. I. Schuster, J. Majer, A. Blais, M. H. Devoret, S. M. Girvin, and R. J. Schoelkopf, Charge-insensitive qubit design derived from the Cooper pair box, Phys. Rev. A **76,** 042319 (2007).

[30] A. Barone and G. Paterno, *Physics and applications of the Josephson effect* (John Wiley Sons, New York, NY, 1982), etc., XVII-529.

[31] G. Oelsner, C. K. Andersen, M. Rehák, M. Schmelz, S. Anders, M. Grajcar, U. Hübner, K. Mølmer, and E. Il'ichev, Detection of Weak Microwave Fields with an Underdamped Josephson Junction, Phys. Rev. Appl. **7,** 014012 (2017).

[32] Ya. Greenberg, Theory of the voltage-current characteristic of high TC DC SQUID, Phys. C **371,** 156 (2002).

[33] M. D. Reed, L. DiCarlo, B. R. Johnson, L. Sun, D. I. Schuster, L. Frunzion, and R. J. Schoelkopf, High-Fidelity Readout in Circuit Quantum Electrodynamics Using the Jaynes-Cummings Nonlinerity, Phys. Rev. Lett. **105,** 173601 (2010).

[34] F. Hirayama, T. Irimatsugawa, H. Yamamori, S. Kohjiro, A. Sato, S. Nagasawa, D. Fukuda, H. Sasaki, M. Hidaka, Y. Sato, M. Ohno, and H. Takahashi, Interchannel crosstalk and nonlinearity of microwave SQUID multiplexers, IEEE Trans. Appl. Supercond. **27,** 4 (2017).